

RED SUPERGIANTS AS COSMIC ABUNDANCE PROBES: THE FIRST DIRECT METALLICITY DETERMINATION OF NGC 4038 IN THE ANTENNAE

C. LARDO¹, B. DAVIES¹, R-P. KUDRITZKI^{2,3}, J. Z. GAZAK², C. J. EVANS⁴, L. R. PATRICK⁵, M. BERGEMANN⁶, B. PLEZ⁷

Draft version September 17, 2015

ABSTRACT

We present a direct determination of the stellar metallicity in the close pair galaxy NGC 4038 ($D = 20$ Mpc) based on the quantitative analysis of moderate resolution KMOS/VLT spectra of three super star clusters (SSCs). The method adopted in our analysis has been developed and optimised to measure accurate metallicities from atomic lines in the J -band of single red supergiant (RSG) or RSG-dominated star clusters. Hence, our metallicity measurements are not affected by the biases and poorly understood systematics inherent to *strong line* H II methods which are routinely applied to massive data sets of galaxies. We find $[Z] = +0.07 \pm 0.03$ and compare our measurements to H II strong line calibrations. Our abundances and literature data suggest the presence of a flat metallicity gradient, which can be explained as redistribution of metal-rich gas following the strong interaction.

Subject headings: galaxies: individual: NGC 4038/39 — galaxies: abundances — galaxies: star clusters: general — methods: analytical — techniques: spectroscopic

1. INTRODUCTION

The metallicity of a galaxy is moderated by the cycling of chemically processed material by stars and any gas exchange between the galaxy and the environment. The central metallicity is correlated with a galaxy mass, a relation which holds information about galaxy formation and evolution (Lequeux et al. 1979; Tremonti et al. 2004; Maiolino et al. 2008; Kudritzki et al. 2012). Additionally, the variation of the metallicity of the galaxy with the distance from the centre keeps track of the complex dynamics of galaxy evolution, as several fundamental physical processes affect metallicity gradients (e.g. Searle 1971; Zaritsky et al. 1994; Garnett et al. 1997; Prantzos & Boissier 2000; Chiappini et al. 2001; Fu et al. 2009; Pilkington et al. 2012; Mott et al. 2013; Kudritzki et al. 2015). Obtaining reliable metallicities in galaxies is crucial to measure and interpret the behaviour of metallicity with radial distance and the mass-metallicity relation. Unfortunately, robust metallicity measurements in galaxies are notoriously problematic to obtain. Metallicity of starburst or star-forming galaxies is routinely measured from H II region emission lines and two main methods are employed: the T_e -based method and the *strong line* method. The T_e -based method uses the flux ratio of auroral to strong lines of the same ion to measure the electron temperature of the gas (Rubin et al. 1994; Lee et al. 2004; Stasińska 2005; Andrews & Martini 2013). However,

temperature sensitive lines are often too weak to be detected in faint distant galaxies and their measurement is challenging even for galaxies in the local universe specifically in the metal-rich regime (Stasińska 2005; Bresolin et al. 2005; Ercolano et al. 2010; Zurita & Bresolin 2012; Gazak et al. 2015). When the electron temperature cannot be determined, one has to resort to abundance indicators based on more readily observable lines. Such *strong line* methods are based on the ratio of the fluxes of the strongest forbidden lines of typically O and H (Pagel et al. 1979; Skillman 1989; McGaugh 1994) which are more easily detected than the weak auroral lines across a wide range of metallicity. Unfortunately, well-known but unexplained systematic uncertainties, that can amount up to ~ 0.7 dex, plague the determination of the metallicity of extragalactic H II regions from nebular spectroscopy (Kewley & Ellison 2008; Bresolin et al. 2009). As a consequence, the chemical abundances derived from strong-line methods display large systematic differences when applied to the same observational data; and only relative metallicity comparisons appear to be reliable if the same calibration is used.

Very promising tracers of the present-day abundances in star-forming galaxies are evolved massive stars. Indeed, a number of nearby galaxies have been studied using blue supergiants (BSGs) and results indicate excellent agreement with abundances obtained from the T_e -based method in H II regions (see Kudritzki et al. 2012, 2013, 2014; Hosek et al. 2014 and references therein).

A growing body of evidence indicates that accurate metallicities over large distance scales as for BSGs can be derived also from red supergiant stars (RSGs). RSGs are young (≤ 20 Myr) and extremely bright stars, i.e. 10^5 - $10^6 L_\odot$ (Humphreys & Davidson 1979). Their flux peaks at $\simeq 1 \mu$ m, therefore they are among the most luminous objects in a galaxy in the near-IR and are ideal candidates for directly measuring extragalactic abundances. RSGs are also very cool stars, with temperatures ranging from 3000 to 5000 K, hence their spectra show numerous absorption features (Allard et al. 2000).

¹ Astrophysics Research Institute, Liverpool John Moores University, IC2, Liverpool Science Park, 146 Brownlow Hill, Liverpool, L3 5RF, UK

² Institute for Astronomy, University of Hawaii, 2680 Woodlawn Drive, Honolulu, HI, 96822, USA

³ University Observatory Munich, Scheinerstr. 1, D-81679, Munich, Germany

⁴ UK Astronomy Technology Centre, Royal Observatory Edinburgh, Blackford Hill, Edinburgh EH9 3HJ, UK

⁵ Institute for Astronomy, University of Edinburgh, Royal Observatory Edinburgh, Blackford Hill, Edinburgh EH9 3HJ, UK

⁶ Max-Planck Institute for Astronomy, 69117, Heidelberg, Germany

⁷ Laboratoire Univers et Particules de Montpellier, Université de Montpellier, CNRS, F-34095 Montpellier, France

Previous techniques to measure metallicity from RSG spectra concentrated on the H -band, where high resolution ($R[\lambda/\delta\lambda] \simeq 20000$) observations are needed to isolate diagnostic atomic lines from molecular absorption (e.g. Davies et al. 2009). Even with the largest available telescopes, the need for high resolution translates prohibitively large exposure times for individual objects at a distance ≥ 1 Mpc. In contrast, the required observing time can be significantly reduced if one focuses on a narrow region in the J -band, where the dominant spectral features are *isolated atomic lines* of Fe and the α elements (Ti, Si, and Mg). Indeed, in this spectral window accurate abundances can be measured even at moderate resolution ($R[\lambda/\delta\lambda] \simeq 3000$).

The J -band method was initially introduced by Davies et al. (2010) for individual RSGs in the Milky Way and has been extended and largely tested by Gazak et al. (2014a) in the association Perseus OB-1. Davies et al. (2015) checked the validity of this method at lower metallicity in the Magellanic Clouds using the VLT/XShooter and Patrick et al. (2015) accurately tailored the reduction/analysis method for KMOS observations of RSGs in NGC 6822. Gazak et al. (2015) obtained metallicities from RSGs across the disk of NGC 300, a spiral galaxy beyond the Local Group, finding a striking agreement with the metallicities recovered from BSG stars and H II-region auroral line measurements.

Interestingly, this technique can be also applied to unresolved star clusters rather than individual stars (Gazak et al. 2013, 2014b). In merging and starburst galaxies intense star formation activity triggers the formation of super star clusters (SSCs), agglomerates of millions of young (≤ 50 Myr) stars. SSCs have masses $\geq 10^5 M_\odot$ and are extremely compact (with radii ≤ 5 pc; Portegies Zwart et al. 2010). Once a SSC reaches an age of $\simeq 7$ Myr, the most massive stars which have not yet exploded as supernovae will be in the RSG phase. For a cluster with an initial mass of $10^5 M_\odot$, there may be more than a hundred RSGs present which dominate the cluster's light output in the near-IR, contributing 90% - 95% of the of the near-IR flux. As their spectra are all very similar in the effective temperature (T_{eff}) range around 4000 K, the combined spectrum can be analysed in the same way as a single RSG spectrum, as shown by Gazak et al. (2014b). Therefore, for SSCs older than 7 Myr the J -band technique can be used to measure metallicity at far greater distances than is possible for single supergiants.

Following this line of investigation, Gazak et al. (2014b) analysed two young SSCs in M 83 (at 4.5 Mpc, Thim et al. 2003) and NGC 6946 (at 5.9 Mpc, Karachentsev et al. 2000), finding metallicities $\simeq 1.5$ -2.0 and $\simeq 0.5 \times$ solar, respectively. This paper further extends the observational baseline and presents quantitative J -band spectroscopy of three SSCs in the close pair galaxy NGC 4838.

NGC 4038 is the main component of the Antennae system (NGC 4038/39), the closest ($\simeq 20$ Mpc)⁸ and youngest example of an ongoing major merger, involving two gas-rich disk galaxies that began to collide $\simeq 200$ -

400 Myr ago (Barnes 1988; Mihos et al. 1993). Galaxy mergers, and their resulting starbursts, are one of the basic building blocks of structure formation in the universe (e.g., Baron & White 1987) and represent an ideal laboratories for close up studies of the physical processes that were important at the peak of cosmic star formation (de Ravel et al. 2009; Bundy et al. 2009). As such, the Antennae has, over the years, been the favourite target for several multi wavelength studies of the effect of tidal interaction (e.g., Whitmore et al. 1999; Fabbiano et al. 2004; Hibbard et al. 2005; Gilbert & Graham 2007; Brandl et al. 2009; Whitmore et al. 2010; Klaas et al. 2010; Whitmore et al. 2014) and numerous N-body and hydrodynamical simulations (e.g., Toomre & Toomre 1972; Barnes 1988; Mihos et al. 1993; Teyssier et al. 2010; Karl et al. 2010).

The bodies of the galaxies are sites of extensive star formation ($\sim 20 M_\odot \text{ yr}^{-1}$; Zhang et al. 2001) producing an IR luminosity of $\log L_{\text{IR}} = 10.76$, which is an order of magnitude lower than ultraluminous infrared galaxies, but still a factor of ~ 5 higher than noninteracting galaxy pairs (see, e.g., Kennicutt et al. 1987). Most of the star formation in this colliding galaxy pair occurs in the form of SSCs (Whitmore & Schweizer 1995; Mirabel et al. 1998; Whitmore et al. 1999; Wilson et al. 2000), with masses up to a few times $10^6 M_\odot$ which are distributed throughout the galaxy (Zhang et al. 2001).

Observational studies demonstrate that in interacting galaxies, the strong metallicity gradient observed in isolated spirals, can be disrupted by gas flows of metal-poor gas from the outer regions towards the centre of the galaxy (e.g. Kewley et al. 2010).

Here we analyse KMOS/VLT spectra of three SSCs to measure the central metallicity and the metallicity gradient across the disk of NGC 4038. This paper is organised in the following way. In Section 2, we summarise the observations and data reduction. We outline our analysis procedure in Section 3. Our results are presented in Section 4. We summarise our main conclusions in Section 5.

2. TARGET SELECTION, OBSERVATIONS AND DATA REDUCTION

Our sample consists of three RSG dominated SSCs, whose coordinates, luminosities, colours, ages are listed in Table 1 together with other useful information. Target SSCs with the appropriate luminosity and colours were selected from optical and near-IR photometry by Whitmore et al. (2010) from the Advanced Camera for Surveys (ACS) and the Near Infrared Camera and Multi-Object Spectrometer (NICMOS) mounted on the HST. Their spatial location across the galaxy is shown in Figure 1. The observations were carried out with KMOS/VLT (Sharples et al. 2013) in April 2014 in visitor mode (PI: Kudritzki: 093.B-0023), with a total exposure time of 6000s split in 20 subsequent exposures.

KMOS is a spectrograph equipped with 24 deployable integral-field units (IFUs) that can be allocated within a $7.2'$ diameter field-of-view (FoV). Each IFU covers a projected area on the sky of about $2.8'' \times 2.8''$, which is sampled by an array of 14×14 spatial pixels (spaxels) each with an angular size of $0.2''$. The 24 IFUs are managed by three identical spectrographs, each one handling eight IFUs. The observations were performed in nod-to-sky mode with the YJ grating, covering the 1.00 - $1.35 \mu\text{m}$ spectral range with a nominal resolution of $R \simeq 3600$ at

⁸ Riess et al. (2011) estimated a distance modulus to the Antennae galaxies of $m-M=31.66 \pm 0.08$ ($\simeq 22.3$ Mpc) from optical and infrared observations of Cepheid variables with the Wide Field Camera 3 (WFC3) on the Hubble Space Telescope (HST).

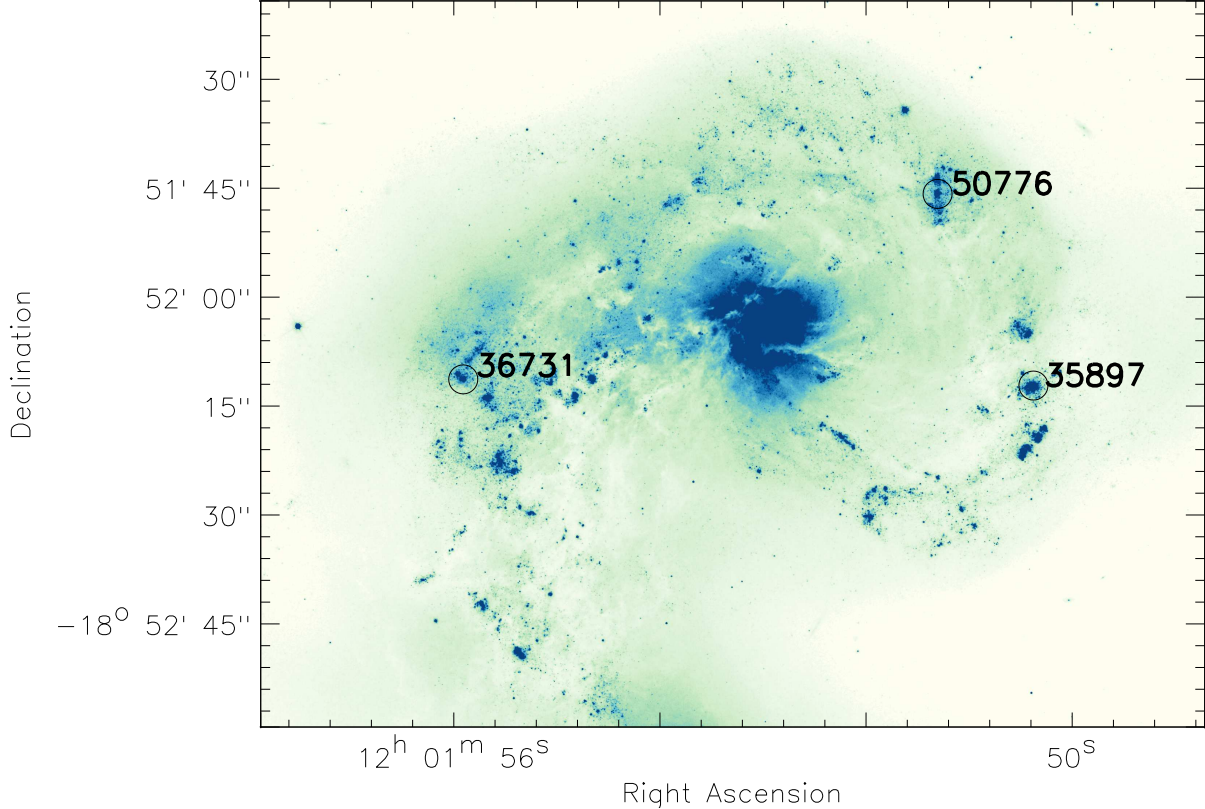


FIG. 1.— The targeted SSCs are overlaid over a HST-ACS F814W image of NGC 4038 retrieved from the Hubble Legacy Archive (<http://hla.stsci.edu/hlview.html>).

TABLE 1
SSCs TARGETED. DATA ARE FROM WHITMORE ET AL. (2010)

ID	R.A.	Decl.	M_V	$m_J^{(a)}$	$E(B - V)$	$\text{Log}\tau/\text{yr}$	Mass (M_\odot)
35897	12:01:50.4453	-18:52:14.223	-11.6	15.8	0.00	7.6	4.5×10^5
36731	12:01:55.9896	-18:52:12.985	-12.5	17.3	0.04	7.6	1.1×10^6
50776	12:01:51.3963	-18:51:47.562	-14.4	16.4	0.04	6.8	1.1×10^6

(a) J magnitudes are from aperture photometry on archival Wide Field Camera 3 images. The typical uncertainty on the J magnitude is ~ 0.1 mags.

the band centre. Observations were carried out using the standard AB AB-like object-sky sequence (i.e. one sky frame for each object frame) in which we offset by $5''$ to sky, and each observation was dithered by up to $0.2''$. During the observations, the average J -band seeing was approximately $1.0''$. In addition to science observations, a standard set of calibration frames were obtained. Since we require high precision absorption line spectroscopy, we observed a telluric standard with the arms in the science configuration (i.e. using the observational template that allows users to observe a standard star in each IFU allocated to a science target). During the observations 7 SSCs were observed, but only three of those have sufficient SNR (≥ 100 , see Gazak et al. 2014a) to be used in our analysis. To reduce the data, we used the standard recipes provided by the by the Software Package for Astronomical Reduction with KMOS (SPARK; Davies et al. 2013). KMOS IFU data cubes were flat fielded, wavelength calibrated, and telluric corrected using the

standard KMOS/esorex routines.

As can be seen in Figure 2, there are significant variations in both spectral resolution and wavelength calibration across the FoV of each IFU as measured from sky emission lines (see below for more details). Left uncorrected, these can introduce sky and telluric cancellation errors into the final spectrum, which can be the source of substantial problems for precision absorption line spectroscopy such as that presented in this paper.

We correct for these effects with a process we call, *kmozgenization* (see also Gazak et al. 2015). We first take the rectified science and sky images *prior* to sky subtraction. At each spaxel in the IFU we fit Gaussian profiles to the sky lines and we use them to determine both the spectral resolution and the higher order wavelength calibration as a function of spatial position. We then smooth the spectra at each position on the IFU down to a lower resolution, set to be $R = 3200^9$. We then extract the

⁹ Though there are regions on the IFU where the spectral reso-

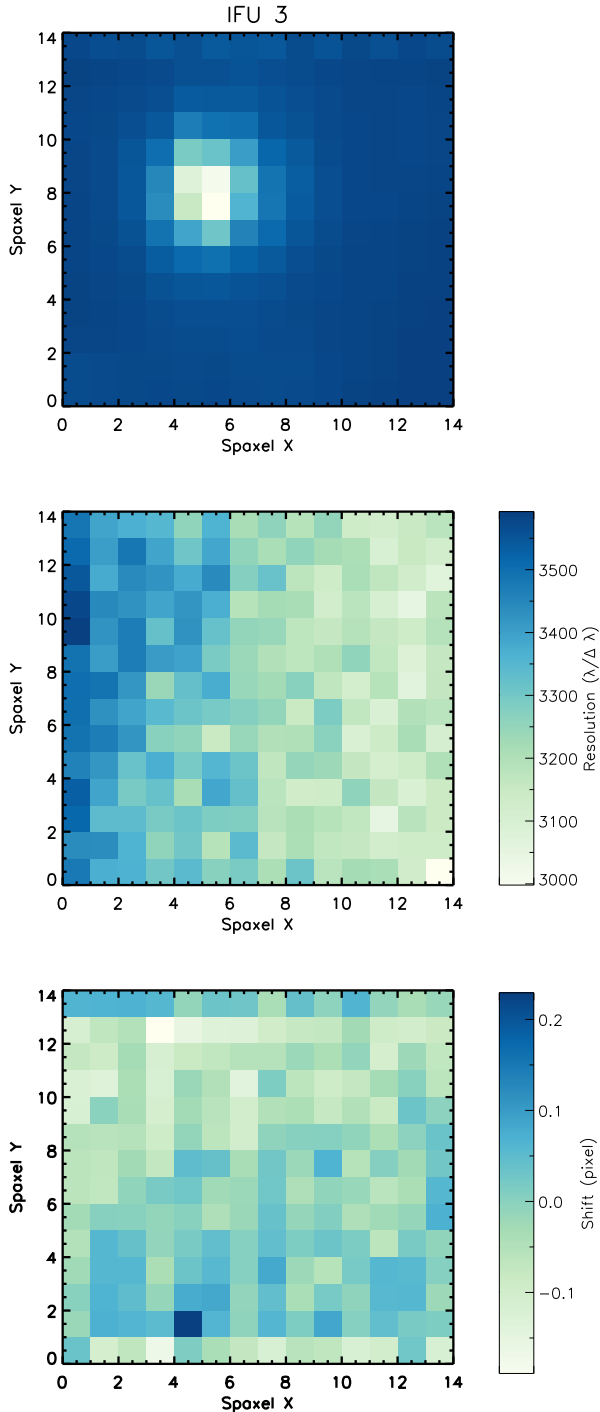


FIG. 2.— Variation of spectral resolution and wavelength calibration across the spatial pixels of a typical KMOS IFU measured from night sky lines. The top panel presents the reconstructed image obtained in a 300 sec exposure. The middle and bottom panels show the variation of spectral resolution and the wavelength shifts (in pixel) across the spaxels, respectively.

lution is below $R = 3200$, the pixels within the extraction aperture are always above this value.

spectrum of the science target from an aperture with radius 1.5 spaxels around the flux peak. This narrow aperture minimises errors due to spatial non-uniformity, at the slight expense of discarding flux from the wings of the point-spread function. When the source is extracted, the wavelength axis is updated to include the higher order correction determined from the sky lines *without* interpolating the spectrum onto a new wavelength axis, as this can introduce numerical noise. The associated sky spectrum is extracted in the same way, and is subtracted from the science spectrum.

Since the wavelength calibration can change slightly throughout the night due to the rotation of the instrument, each sky-subtracted science spectrum can have a different wavelength axis. To account for this, the normalised spectra are co-added onto a master wavelength axis whereby the flux at wavelength λ_i in the master spectrum is a weighted mean of the fluxes in the individual spectra which have wavelengths between λ_{i-1} and λ_{i+1} . Rejection of outliers is also performed at this stage, to eliminate cosmic rays and bad pixels.

Finally, we experimented with altering the output spectral resolution to test the robustness of our method. We found that the best-fitting parameters (see next section) were stable to well within the fitting errors as long as the output resolution was greater than $R = 3100$.

3. ANALYSIS

Metallicity $[Z]$ (normalised to Solar values, $[Z] = \log(Z/Z_\odot)$ ¹⁰, effective temperature (T_{eff}), surface gravity ($\log g$) and microturbulence (ξ) have been derived as extensively explained in the previous papers of this series (e.g. Davies et al. 2010; Gazak et al. 2014b,a; Davies et al. 2015; Patrick et al. 2015; Gazak et al. 2015). In particular, the studies of Davies et al. (2010), Gazak et al. (2014a), and Gazak et al. (2015) demonstrate the applicability of the technique to objects with roughly solar chemical enrichment.

Atmospheric parameters and metallicity were derived by comparing the observed spectra with a grid of single-star synthetic spectra degraded to the same spectral resolution as those observed. Model atmospheres were calculated with the MARCS code (Gustafsson et al. 2008), where the range of parameters are defined in Table 2. The synthetic spectra were computed using the updated version of the SIU code, as described in Bergemann et al. (2012). Departures from local thermodynamic equilibrium (LTE) for Fe I, Mg I, Si I, and Ti I lines were also included (Bergemann et al. 2012, 2013, 2015). All other lines including the weak molecular contributions are calculated in LTE. The best fit model has been derived through a χ^2 -minimisation between the observed spectrum and a template spectrum at each point in the model grid, taking into account possible shifts and variations in instrumental spectral resolution between the observed spectra and the models. The methodology for finding the best-fitting model is described in detail by

¹⁰ We measure Fe, Mg, Si, and Ti abundances from individual lines and assume this is representative of the metallicity Z . While the assumption of a solar-scaled composition appears reasonable, we note that the errors deriving from the assumption of a solar-scaled composition rather than an $[\alpha/\text{Fe}]$ -enhanced one has a little impact on the metallicity measurements, i.e. well within the quoted errors on metallicity.

TABLE 2
MODEL GRID

Parameter	Units	Grid Min	Grid Max	Grid Step
T_{eff}	K	3400	4400	100
$\log g$	dex	-1.0	+ 1.0	0.5
$[Z]$	dex	-1.00	+1.00	0.25
ξ	km s ⁻¹	1.0	5.0	1.0

Gazak et al. (2014a) and Gazak et al. (2015) which analyse 11 RSGs in Perseus OB-1 ($[Z] = -0.04 \pm 0.08$) and 27 RGGs in NGC 300 ($[Z] = -0.03 \pm 0.05$), respectively. Briefly, we measured best fit parameters by isolating 2D planes in each parameter pair combination which contain the minimum. As a result, two parameters are locked to the best fit values in each of the six slices, while allowing the other two parameters to vary. We thus constructed a 2D plane of minimum χ^2 values as a function of the two fixed parameters and draw contours of equal χ^2 . This procedure is repeated for all the planes, and the measurements of each parameter are finally averaged to derive best fit parameters. An example of this is shown in Figure 4. Figure 4 shows the degeneracy between $[Z]$ and $\log g$, while demonstrating how soundly constrained are T_{eff} and ξ . We refer again to Gazak et al. (2014a) and Gazak et al. (2015) for a thorough discussion of the sensitivity of diagnostic lines to the free parameters (e.g. T_{eff} , $\log g$, ξ , and $[Z]$) and the complete error analysis. The best-fitting parameters are listed in Table 3, along with their associated uncertainties.

4. RESULTS

4.1. Metallicity

Figure 3 displays fits of the metal lines with the best fitting model spectra in our diagnostic spectral window. The match to the stellar lines used to derive metallicity (labelled in the same Figure) is very good, and also the fit to the unresolved features of the pseudo-continuum is remarkable. The spectral feature at $1.205\mu\text{m}$ is due to a poorly removed telluric line.

Table 3 summarises the derived stellar parameters and metallicities. The average metallicity for our sample of 3 SSCs is $[Z] = +0.07 \pm 0.03$ ($\sigma=0.05$ dex), in agreement with previous measurements based on different diagnostics. Solar metallicity has been inferred by Mengel et al. (2002) from the analysis of the metallicity sensitive Mg I line at 8806.8\AA in a handful of SSCs. Bastian et al. (2009) measure the strong emission lines in H II regions¹¹ to derive metallicities of 16 SSCs, finding a slightly super-solar value (see Figure 5). They use the equivalent width ratios of the collisional excited $[\text{O II}]\lambda 3727$ and $[\text{O III}]\lambda 4959$, 5007 lines relative to the $\text{H}\beta$ Balmer series recombination lines to estimate the gas-phase oxygen abundance, i.e. the R23 line ratio. Moreover, they adopt the analysis method from Kobulnicky & Kewley 2004 (hereafter KK04) and a solar abundances of $12 + \log(\text{O}/\text{H})_{\odot} = 8.89$ (Edmunds & Pagel 1984), which is 0.2 higher than our adopted solar metallicity, i.e. $12 + \log(\text{O}/\text{H})_{\odot} = 8.69$ (Asplund et al. 2009). Bastian et

TABLE 3
SPECTRAL FITS

SSC	T_{eff} (K)	$\log g$ (dex)	ξ (km/s)	Z (dex)
35897	3890 ± 50	0.4 ± 0.2	1.7 ± 0.2	0.01 ± 0.07
36731	3750 ± 50	0.6 ± 0.2	2.0 ± 0.2	0.09 ± 0.08
50776	3770 ± 50	0.5 ± 0.2	2.0 ± 0.2	0.11 ± 0.07

al. (2006) presented a study of several SSCs from VIMOS/VLT spectra. However, they do not have available the $[\text{O II}]\lambda 3727$ emission line strength to measure the O/H ratio. Therefore, they use the Vacca & Conti (1992) calibration that relies on the R3 ratio. Since this calibration does not include the contribution from another ionised species of oxygen (i.e. $[\text{O II}]$), the abundances presented by Bastian et al. (2006) should be taken with caution, as stated by the authors themselves. In the following, we do not discuss those abundances further¹².

4.2. Metallicity gradient

Any sizeable galaxy-galaxy interaction affects the metallicity distribution of the galaxies involved. Observational studies of interacting or close pair galaxies have shown that these undergo nuclear metal dilution owing to gas inflow, resulting in a significant flattening of their gas-phase metallicity gradients (Lee et al. 2004; Trancho et al. 2007; Chien et al. 2007; Kewley et al. 2006; Rupke et al. 2008; Ellison et al. 2008; Michel-Dansac et al. 2008; Kewley et al. 2010; Rich et al. 2012; Sánchez et al. 2014; Rosa et al. 2014).

In the last decade, several studies have been published analysing the influence of different levels of interactions in the metallicity distribution of galaxies. Kewley et al. (2010) present the first systematic analysis of metallicity gradients in close pairs. They obtain spectra of star forming regions in eight galaxies in close pair systems and find that the metallicity gradients are significantly shallower than the gradients in isolated spirals. Krabbe et al. (2008) study the kinematics and physical properties of the minor merger AM2306–721. They report a clear metallicity gradient across the disc of the main galaxy, while the secondary, less massive companion shows a relatively homogeneous oxygen abundance. A nearly flat radial gradient was measured for both components of the system AM 2322–821 by (Krabbe et al. 2011). Werk et al. (2011) find that the interacting galaxies in their spectroscopic sample have flat oxygen abundance gradients out to large projected radii. A flat metallicity gradient has also been reported for NGC 1512, a barred spiral in a close interaction with a blue compact dwarf companion (Bresolin et al. 2012) and NGC 92, the largest galaxy in Robert’s quartet (Torres-Flores et al. 2014). Rosa et al. (2014) measure oxygen abundance gradients from H II regions located in 11 galaxies in eight systems of close pairs from Gemini/GMOS spectra, finding metal-

¹¹ As the lifetimes of RSGs are ≤ 50 Myr, their metallicities are expected to be representative of the clouds from which they are formed.

¹² Note that two of the SSCs reanalysed in Bastian et al. (2006) were also observed in Bastian et al. (2009), and one on our target (36731) is in common with the Bastian et al. (2006) sample; i.e. their complex 3. For the SSC in common with our sample, Bastian et al. (2006) estimate a metallicity of $Z=0.45 Z_{\odot}$, with an estimated intrinsic uncertainty of ± 0.2 in $\log(\text{O}/\text{H})$ (Edmunds & Pagel 1984) and a solar oxygen abundance of $12 + \log(\text{O}/\text{H})_{\odot} = 8.91$ (Meyer 1985), which is compatible with our measurement.

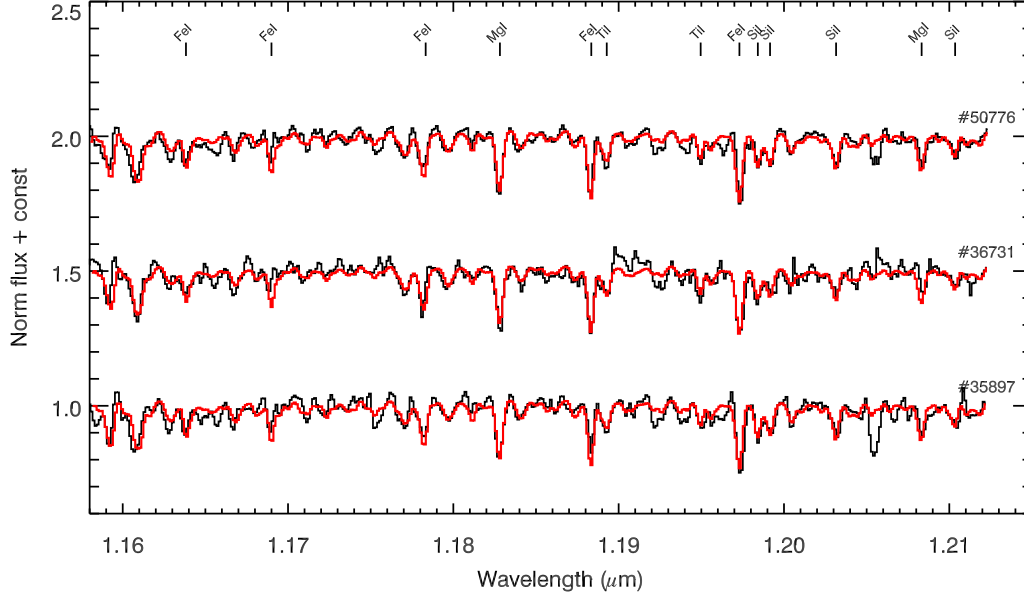


FIG. 3.— Spectra of the targeted SSCs in the J -band window, along with the best-fit spectra (red lines).

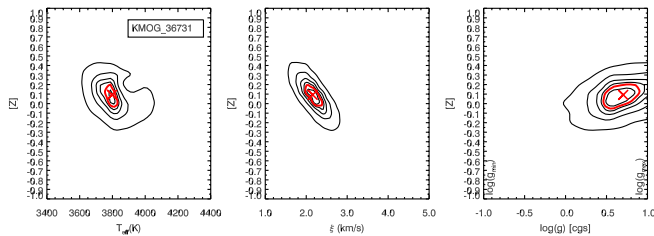


FIG. 4.— Planes through the model grid showing the degeneracy between the parameters for the analysed SSCs. The black contours show contours of equal χ^2 , and are drawn at levels of $\chi^2_{min} + (1, 2, 3, 5, 10)$. The red contour is drawn at $\chi^2 = \chi^2_{min} + 3$ which indicates our 1σ uncertainty. The x -axis limits on the right-hand plot are the minimum and maximum possible values of $\log g$ allowed by the object temperature and luminosity.

licity gradients significantly flatter than those observed in typical isolated spiral galaxies. Finally, Sánchez et al. (2014) derive radial gradients of the oxygen abundance in ionised gas in 306 nearby galaxies observed by the CALIFA survey. Using a large and homogeneous sample of more than 40 mergers/interacting systems, they find statistical evidence of a flattening in the abundance gradients in interacting systems at any interaction stage.

The absence of an abundance gradient in interacting galaxies is explained by invoking efficient mixing of low-metallicity gas from the outer parts with the metal-rich gas of the centre of the galaxy. Smoothed particle hydrodynamic merger simulations of Barnes & Hernquist (1996) and Mihos & Hernquist (1996) predict that in interacting galaxies the strong tidal interaction during encounters can aid disk to develop bars. In such barred disks, low-metallicity gas from the outskirts can efficiently flow towards the central regions at higher metallicity funnelled by bar instabilities, flattening the initial radial metallicity gradient (Hibbard & van Gorkom 1996; Georgakakis et al. 2000; Rampazzo et al. 2005; Rupke et al. 2005; Iono et al. 2005; Emonts et al. 2006; Martin 2006; Cullen et al. 2007).

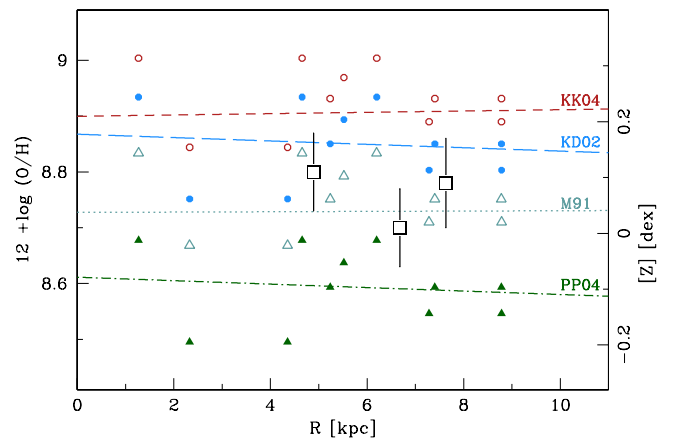


FIG. 5.— Direct metallicities from the SSC analysis (large squares) are shown together with the H II region metal abundances by Bastian et al. (2009) as a function of galactocentric radius. Small symbols are the abundances obtained from different strong-line calibrations to the Bastian et al. 2009 data: Kobulnicky & Kewley 2004 (KK04; red empty circles, adopted by Bastian et al. 2009), Kewley & Dopita 2002 (KD02; blue filled circles), McGaugh 1991 (M91; teal empty triangles), and Pettini & Pagel 2004 (PP04; green filled triangles).

We plot our direct metallicity measurements against the radial distance from the centre in Figure 5. Galactocentric radii are computed using the direct distance to the galaxy centre, where the galaxy centre is defined using Two Micron All Sky Survey (2MASS) images. Distances take inclination into account ($i=56.56^\circ$) using the optical diameters from Lauberts & Valentijn (1989). A weighted linear regression to our SSC data yields a central metallicity of $+0.17 \pm 0.23$ dex and a flat gradient (-0.02 ± 0.03 dex kpc^{-1}), consistent with observations and N-body simulations of interacting systems.

4.3. Strong-line Abundances

Even though the original observations do not include all the different metallicity indicators, we can still com-

pare our direct SSC metallicities to strong-line calibrations, as applied to the Bastian et al. (2009) data¹³. SSCs metallicities refer to the combined abundances Mg, Si, Ti, and Fe (see Section 3, where the individual abundances are scaled relative to the solar abundance pattern). In comparing the metallicities from the SSCs with the oxygen abundances from the H II regions, we assume that the oxygen abundances of the SSCs scale with metallicity, and that the solar metallicity value corresponds to $12 + \log(\text{O}/\text{H})_{\odot} = 8.69$ (Asplund et al. 2009).

Figure 5 illustrates how four different strong-line calibrations, as applied to the Bastian et al. (2009) sample, compare to our metallicities. We consider the R23 = $([\text{O II}]\lambda 3727 + [\text{O III}]\lambda\lambda 4959, 5007)/\text{H}\beta$ indicator, with the theoretical predictions by McGaugh 1991 (M91) and KK04, i.e. the calibration used by Bastian et al. (2009), the calibration for the $[\text{N II}]\lambda 6583/[\text{O II}]\lambda 3727$ diagnostic presented in Kewley & Dopita 2002 (KD02), and O3N2 = $\log([\text{O III}]\lambda 5007/\text{H}\beta)/([\text{N II}]\lambda 6584/\text{H}\alpha)$, empirically calibrated on H II regions with T_e -based metallicities by Pettini & Pagel 2004 (PP04). The estimated accuracy of the all these calibrations is $\simeq 0.10 - 0.15$ dex. We use the coefficients of the polynomial from Table 3 in Kewley & Ellison (2008) to convert metallicities from the KK04 calibration into a metallicity that is consistent with other calibrations using a third-order polynomial.

The abundances that result from the application of these different indicators and calibrations, together with the direct SSC abundances derived in Section 3, are shown as a function of the distance from the centre of NGC 4038 in Figure 5. A linear least-square fit to the data is also shown for each method. While all the considered methods imply a flat metallicity gradient, both the KK04 and KD02 calibrations provide metallicities that are larger than those from SSCs, while the PP04 calibration give metallicities that are lower than ours. Figure 5 also shows that the M91-based metallicities better agree to the direct metallicity determination. However, we stress that only the KK04 and M91 calibrations rely on the set of emission lines actually observed in Bastian et al. (2009) data, i.e. $[\text{O II}]\lambda 3727$, $[\text{O III}]\lambda 4959$, $[\text{O III}]\lambda 5007$, $\text{H}\beta$; while both the PP04 and KD02 calibrations include diagnostic lines (i.e. $[\text{N II}]\lambda 6583$, $\text{H}\alpha$) not present in the original Bastian et al. (2009) spectra. Moreover, we note that all the abundances from Figure 5 agree within $\pm 2\sigma$. As a result, we caution that the comparison presented in Figure 5 is purely qualitative, because we are not comparing actual measurements but using instead empirically derived metallicity conversions with their associated uncertainties.

The data suggest the presence of a flat abundance gradient, however they sample only a small range in distances from the galaxy centre. Indeed, the number of SSCs observed should be increased considerably, especially in the inner regions, in order to test for radial variations and confirm whether the metallicity gradient is as

shallow as found by Bastian et al. (2009) and suggested by our data.

Knowledge of the chemical composition of galaxies is fundamental to trace back the history of cosmic chemical enrichment and understand the processes at work in galaxy formation and evolution. Chemical abundances in extragalactic environments are commonly based on H II region optical emission-line ratios. Numerous relations have been proposed to convert diagnostic emission line ratios into metallicity (see for a review Kewley & Dopita 2002). Nonetheless, comparisons between abundances obtained from different calibrations show a systematic offset in metallicity estimates, that can amount up to ~ 0.7 dex (Bresolin 2008; Kewley & Ellison 2008).

We have developed a new method to avoid these calibration issues by performing quantitative spectroscopy of RSG stars or RSG-dominated SSCs in external galaxies. In this paper we use this J -band technique on KMOS spectra of three SSCs in NGC 4038 to measure precise metallicities (see Davies et al. 2010; Gazak et al. 2014b,a, 2015; Davies et al. 2015; Patrick et al. 2015). We find an average metallicity of $[Z] = +0.07 \pm 0.03$ ($\sigma = 0.05$ dex). Given the uncertainties, this is in good agreement with the results from H II regions data by Bastian et al. (2009), when the McGaugh (1991) calibration is used to determine abundances. Furthermore, we find no evidence for a metallicity gradient. However, a larger systematic study of RSGs is needed to assess the presence (or not) of a metallicity gradient among the young population within this merger galaxy pair.

With the multi-object near IR spectrographs such as KMOS/VLT and MOSFIRE/Keck we can now investigate the chemical evolution of galaxies out to ~ 7 Mpc from individual RSG stars (i.e. Davies et al. 2010, 2015; Patrick et al. 2015; Gazak et al. 2015). Using the same technique on SSC, we here measure metallicity as precise as ~ 0.10 dex out to the astonishing distance of ~ 20 Mpc in less than one night of observations. This opens new windows for extragalactic spectroscopy. Indeed, the J -band method will allow us to quantitatively study the chemical evolution of galaxies –up to the Coma cluster– in a way similar to current Galactic studies (Evans et al. 2011), when the next generation of extremely large telescopes, equipped with adaptive optics supported near IR multi-object spectrographs, will be available to the community.

Based on observations made with ESO Telescopes at the La Silla Paranal Observatory under programme ID 093.B-0023. We are very grateful to the anonymous referee who helped us improve our manuscript. RPK and JZG gratefully acknowledge support by the National Science foundation (NSF) under grant AST-1108906. BP thanks the CNRS Programme National de Physique Stellaire for financial support.

Facilities: VLT(KMOS).

REFERENCES

5. SUMMARY
- ¹³ Bastian et al. (2009) assumed that all H II regions belong to the upper branch of the R23 calibration.
- Allard, F., Hauschildt, P. H., & Schwenke, D. 2000, ApJ, 540, 1005
 Andrews, B. H., & Martini, P. 2013, ApJ, 765, 140
 Asplund, M., Grevesse, N., Sauval, A. J., & Scott, P. 2009, ARA&A, 47, 481
 Barnes, J. E., & Hernquist, L. 1996, ApJ, 471, 115

- Barnes, J. E. 1988, *ApJ*, 331, 699
- Baron, E., & White, S. D. M. 1987, *ApJ*, 322, 585
- Bastian, N., Emsellem, E., Kissler-Patig, M., & Maraston, C. 2006, *A&A*, 445, 471
- Bastian, N., Trancho, G., Konstantopoulos, I. S., & Miller, B. W. 2009, *ApJ*, 701, 607
- Bergemann, M., Kudritzki, R.-P., Plez, B., et al. 2012, *ApJ*, 751, 156
- Bergemann, M., Kudritzki, R.-P., Würl, M., et al. 2013, *ApJ*, 764, 115
- Bergemann, M., Kudritzki, R.-P., Gazak, Z., Davies, B., & Plez, B. 2015, *ApJ*, 804, 113
- Brandl, B. R., Snijders, L., den Brok, M., et al. 2009, *ApJ*, 699, 1982
- Bresolin, F., Schaerer, D., González Delgado, R. M., & Stasińska, G. 2005, *A&A*, 441, 981
- Bresolin, F. 2008, *The Metal-Rich Universe*, 155
- Bresolin, F., Gieren, W., Kudritzki, R.-P., et al. 2009, *ApJ*, 700, 309
- Bresolin, F., Kennicutt, R. C., & Ryan-Weber, E. 2012, *ApJ*, 750, 122
- Bundy, K., Fukugita, M., Ellis, R. S., et al. 2009, *ApJ*, 697, 1369
- Chiappini, C., Matteucci, F., & Romano, D. 2001, *ApJ*, 554, 1044
- Chien, L.-H., Barnes, J. E., Kewley, L. J., & Chambers, K. C. 2007, *ApJ*, 660, L105
- Cullen, H., Alexander, P., Green, D. A., & Sheth, K. 2007, *MNRAS*, 376, 98
- Davies, B., Origlia, L., Kudritzki, R.-P., et al. 2009, *ApJ*, 694, 46
- Davies, B., Kudritzki, R.-P., & Figer, D. F. 2010, *MNRAS*, 407, 1203
- Davies, B., Kudritzki, R.-P., Gazak, Z., et al. 2015, *ApJ*, 806, 21
- Davies, R. I., Agudo Berbel, A., Wierorrek, E., et al. 2013, *A&A*, 558, AA56
- de Ravel, L., Le Fèvre, O., Tresse, L., et al. 2009, *A&A*, 498, 379
- Edmunds, M. G., & Pagel, B. E. J. 1984, *MNRAS*, 211, 507
- Ellison, S. L., Patton, D. R., Simard, L., & McConnachie, A. W. 2008, *AJ*, 135, 1877
- Emonts, B. H. C., Morganti, R., Tadhunter, C. N., et al. 2006, *A&A*, 454, 125
- Ercolano, B., Wesson, R., & Bastian, N. 2010, *MNRAS*, 401, 1375
- Evans, C. J., Davies, B., Kudritzki, R.-P., et al. 2011, *A&A*, 527, AA50
- Fabbiano, G., Baldi, A., King, A. R., et al. 2004, *ApJ*, 605, L21
- Fu, J., Hou, J. L., Yin, J., & Chang, R. X. 2009, *ApJ*, 696, 668
- Garnett, D. R., Shields, G. A., Skillman, E. D., Sagan, S. P., & Dufour, R. J. 1997, *ApJ*, 489, 63
- Gazak, J. Z., Bastian, N., Kudritzki, R.-P., et al. 2013, *MNRAS*, 430, L35
- Gazak, J. Z., Davies, B., Kudritzki, R., Bergemann, M., & Plez, B. 2014a, *ApJ*, 788, 58
- Gazak, J. Z., Davies, B., Bastian, N., et al. 2014b, *ApJ*, 787, 142
- Gazak, J. Z., Kudritzki, R., Evans, C., et al. 2015, *ApJ*, 805, 182
- Georgakakis, A., Forbes, D. A., & Norris, R. P. 2000, *MNRAS*, 318, 124
- Gilbert, A. M., & Graham, J. R. 2007, *ApJ*, 668, 168
- Gustafsson, B., Edvardsson, B., Eriksson, K., et al. 2008, *A&A*, 486, 951
- Hibbard, J. E., & van Gorkom, J. H. 1996, *AJ*, 111, 655
- Hibbard, J. E., Bianchi, L., Thilker, D. A., et al. 2005, *ApJ*, 619, L87
- Hosek, M. W., Jr., Kudritzki, R.-P., Bresolin, F., et al. 2014, *ApJ*, 785, 151
- Humphreys, R. M., & Davidson, K. 1979, *ApJ*, 232, 409
- Iono, D., Yun, M. S., & Ho, P. T. P. 2005, *ApJS*, 158, 1
- Karachentsev, I. D., Sharina, M. E., & Huchtmeier, W. K. 2000, *A&A*, 362, 544
- Karl, S. J., Naab, T., Johansson, P. H., et al. 2010, *ApJ*, 715, L88
- Kennicutt, R. C., Jr., Roettiger, K. A., Keel, W. C., van der Hulst, J. M., & Hummel, E. 1987, *AJ*, 93, 1011
- Kewley, L. J., & Dopita, M. A. 2002, *ApJS*, 142, 35
- Kewley, L. J., & Ellison, S. L. 2008, *ApJ*, 681, 1183
- Kewley, L. J., Geller, M. J., & Barton, E. J. 2006, *AJ*, 131, 2004
- Kewley, L. J., Rupke, D., Zahid, H. J., Geller, M. J., & Barton, E. J. 2010, *ApJ*, 721, L48
- Klaas, U., Nielbock, M., Haas, M., Krause, O., & Schreiber, J. 2010, *A&A*, 518, LL44
- Krabbe, A. C., Pastoriza, M. G., Winge, C., Rodrigues, I., & Ferreira, D. L. 2008, *MNRAS*, 389, 1593
- Krabbe, A. C., Pastoriza, M. G., Winge, C., et al. 2011, *MNRAS*, 416, 38
- Kudritzki, R.-P., Urbaneja, M. A., Gazak, Z., et al. 2012, *ApJ*, 747, 15
- Kudritzki, R.-P., Urbaneja, M. A., Gazak, Z., et al. 2013, *ApJ*, 779, LL20
- Kudritzki, R.-P., Urbaneja, M. A., Bresolin, F., Hosek, M. W., Jr., & Przybilla, N. 2014, *ApJ*, 788, 56
- Kudritzki, R.-P., Ho, I.-T., Schrubba, A., et al. 2015, *MNRAS*, 450, 342
- Kobulnicky, H. A., & Kewley, L. J. 2004, *ApJ*, 617, 240
- Lauberts, A., & Valentijn, E. A. 1989, *The Messenger*, 56, 31
- Lee, J. C., Salzer, J. J., & Melbourne, J. 2004, *ApJ*, 616, 752
- Lequeux, J., Peimbert, M., Rayo, J. F., Serrano, A., & Torres-Peimbert, S. 1979, *A&A*, 80, 155
- Maiolino, R., Nagao, T., Grazian, A., et al. 2008, *A&A*, 488, 463
- Martin, C. L. 2006, *ApJ*, 647, 222
- McGaugh, S. S. 1991, *ApJ*, 380, 140
- McGaugh, S. S. 1994, *ApJ*, 426, 135
- Mengel, S., Lehnert, M. D., Thatte, N., & Genzel, R. 2002, *A&A*, 383, 137
- Meyer, J.-P. 1985, *ApJS*, 57, 173
- Michel-Dansac, L., Lambas, D. G., Alonso, M. S., & Tissera, P. 2008, *MNRAS*, 386, L82
- Mihos, J. C., & Hernquist, L. 1996, *ApJ*, 464, 641
- Mihos, J. C., Bothun, G. D., & Richstone, D. O. 1993, *ApJ*, 418, 82
- Mirabel, I. F., Vigroux, L., Charmandaris, V., et al. 1998, *A&A*, 333, L1
- Mott, A., Spitoni, E., & Matteucci, F. 2013, *MNRAS*, 435, 2918
- Pagel, B. E. J., Edmunds, M. G., Blackwell, D. E., Chun, M. S., & Smith, G. 1979, *MNRAS*, 189, 95
- Patrick, L. R., Evans, C. J., Davies, B., et al. 2015, *ApJ*, 803, 14
- Pettini, M., & Pagel, B. E. J. 2004, *MNRAS*, 348, L59
- Pilkington, K., Few, C. G., Gibson, B. K., et al. 2012, *A&A*, 540, A56
- Portegies Zwart, S. F., McMillan, S. L. W., & Gieles, M. 2010, *ARA&A*, 48, 431
- Prantzos, N., & Boissier, S. 2000, *MNRAS*, 313, 338
- Rampazzo, R., Plana, H., Amram, P., et al. 2005, *MNRAS*, 356, 1177
- Rich, J. A., Torrey, P., Kewley, L. J., Dopita, M. A., & Rupke, D. S. N. 2012, *ApJ*, 753, 5
- Riess, A. G., Macri, L., Casertano, S., et al. 2011, *ApJ*, 730, 119
- Rosa, D. A., Dors, O. L., Krabbe, A. C., et al. 2014, *MNRAS*, 444, 2005
- Rubin, R. H., Simpson, J. P., Lord, S. D., et al. 1994, *ApJ*, 420, 772
- Rupke, D. S., Veilleux, S., & Sanders, D. B. 2005, *ApJS*, 160, 115
- Rupke, D. S. N., Veilleux, S., & Baker, A. J. 2008, *ApJ*, 674, 172
- Sánchez, S. F., Rosales-Ortega, F. F., Iglesias-Páramo, J., et al. 2014, *A&A*, 563, AA49
- Skillman, E. D. 1989, *ApJ*, 347, 883
- Searle, L. 1971, *ApJ*, 168, 327
- Sharples, R., Bender, R., Agudo Berbel, A., et al. 2013, *The Messenger*, 151, 21
- Stasińska, G. 2005, *A&A*, 434, 507
- Teyssier, R., Chapon, D., & Bournaud, F. 2010, *ApJ*, 720, L149
- Thim, F., Tammann, G. A., Saha, A., et al. 2003, *ApJ*, 590, 256
- Toomre, A., & Toomre, J. 1972, *ApJ*, 178, 623
- Trancho, G., Bastian, N., Miller, B. W., & Schweizer, F. 2007, *ApJ*, 664, 284
- Tremonti, C. A., Heckman, T. M., Kauffmann, G., et al. 2004, *ApJ*, 613, 898
- Torres-Flores, S., Scarano, S., Mendes de Oliveira, C., et al. 2014, *MNRAS*, 438, 1894
- Vacca, W. D., & Conti, P. S. 1992, *ApJ*, 401, 543
- Werk, J. K., Putman, M. E., Meurer, G. R., & Santiago-Figueroa, N. 2011, *ApJ*, 735, 71
- Wilson, C. D., Scoville, N., Madden, S. C., & Charmandaris, V. 2000, *ApJ*, 542, 120
- Whitmore, B. C., & Schweizer, F. 1995, *AJ*, 109, 960
- Whitmore, B. C., Zhang, Q., Leitherer, C., et al. 1999, *AJ*, 118, 1551

- Whitmore, B. C., Chandar, R., Schweizer, F., et al. 2010, *AJ*, 140, 75
- Whitmore, B. C., Brogan, C., Chandar, R., et al. 2014, *ApJ*, 795, 156
- Zaritsky, D., Kennicutt, R. C., Jr., & Huchra, J. P. 1994, *ApJ*, 420, 87
- Zhang, Q., Fall, S. M., & Whitmore, B. C. 2001, *ApJ*, 561, 727
- Zurita, A., & Bresolin, F. 2012, *MNRAS*, 427, 1463